A Dynamic Lunar Spectral Irradiance Data Set for NPOESS/VIIRS Day/Night Band Nighttime Environmental Applications

Steven D. Miller and Robert E. Turner

Abstract—In anticipation of the first fully calibrated nighttime low-light measurements from the National Polar-orbiting Operational Environmental Satellite System's Visible/Infrared Imager/Radiometer Suite (VIIRS) Day/Night Band (DNB), a simple model has been developed for quantifying the highly variable top-of-atmosphere spectral irradiance (in watts per square meter per micrometer) from Earth's only natural satellite—the Moon. Based on the state-of-the-art in solar source observations, lunar spectral albedo data, and an account for the time-varying Sun/Earth/Moon geometry and lunar phase, the model produces 1-nm resolution irradiance spectra over the interval [0.3, 1.2 μm] for a given date and time. Convolving the spectra with the sensor response function of the VIIRS/DNB allows for the conversion from measurements of upwelling radiance to equivalent lunar reflectance [i.e., 0%–100%]—enabling quantitative nighttime multispectral applications that have heretofore been restricted to the daytime hours for lack of visible reflectance information. In the interest of advancing research in nighttime environments, we present here the development and validation of a lunar spectral irradiance database, supply auxiliary data and tools necessary for computing temporally dependent values, and discuss some of the environmental applications enabled by this utility.

Index Terms—Image sensors, moon, National Polar-orbiting Operational Environmental Satellite System (NPOESS), remote sensing, satellite applications, spectral irradiance, Visible/Infrared Imager/Radiometer Suite (VIIRS) day/night band.

I. Introduction

TO DATE, the application of visible-band (e.g., 0.4–0.7 μm) satellite radiometers has been limited almost exclusively to daytime applications, when significant levels of visible radiation are available. Here, measurements of sunlight reflecting off of various constituents of the Earth/atmosphere system provide information useful for both environmental

visualization (imagery) and characterization (i.e., relating these observations to physical and optical properties of the scattering media). In terms of hardware, conventional visible-band sensors utilize silicon photodetectors, which offer adequate sensitivity to a broad range of daytime visible radiation (e.g., spanning radiances on the order of $10^0 - 10^2$ W · $m^{-2} \cdot sr^{-1} \cdot \mu m^{-1}$). Contemporary examples of such sensors include the visible channels on the Advanced Very High Resolution Radiometer, the MODerate Resolution Imaging Spectroradiometer (MODIS), and the Geostationary Operational Environmental Satellite (GOES) imager.

Visible-band radiation is also present during the nighttime hours, albeit typically at much lower levels and occurring over small areas (relative to satellite pixels on the order of 1 km^2). These weak signals require a high degree of amplification in order to detect from the satellite platform. Examples of nocturnal lights include both artificial (e.g., city lights, oil platform gas flares, and fishing boat flood lights) and natural (moonlight, lightning flashes, aurora, and bioluminescence) sources. Whereas a significant body of research has centered on anthropogenic activities as inferred from city light mapping (see, e.g., [1]–[5]), relatively few studies examine natural-light applications (see, e.g., [6]–[9]).

Of particular interest to nighttime environmental characterization, and the subject of this paper, is the potential use of moonlight in the same context as the Sun—enabling equivalent daytime multispectral applications that require measurements of visible reflectance. Doing so requires an accurate characterization of the downwelling top-of-atmosphere (TOA) lunar spectral irradiance. However, unlike the downwelling TOA solar irradiance which varies mostly because of Sun/Earth (S/E) distance, the lunar irradiance varies dramatically according to the variable lunar phase (New Moon to Full Moon) and Sun/Earth/Moon (S/E/M) geometry over the seasons and course of the lunar cycle. Considering that the maximum possible TOA lunar spectral irradiance [attained at a nearly Full Moon that coincides with the closest points between the Moon's orbit about the Earth (perigee) and Earth's orbit about the Sun (perihelion)] is only 5–6 mW · $m^{-2} \cdot sr^{-1} \cdot \mu m^{-1}$ (compared to TOA solar spectral irradiances topping out at over 2000 W · $m^{-2} \cdot sr^{-1} \cdot \mu m^{-1}$), a high degree of instrument sensitivity and radiometric resolution is required to provide useful measurements of reflected moonlight.

The first sensor to exploit moonlight reflectance for meteorological applications was the Defense Meteorological Satellite Program (DMSP). Being a Department of Defense (DoD) program that was initially classified upon its inception in the

mid-1960s, the DMSP was designed in part to supply military analysts with a means to producing global cloud cover analyses during both day and night hours. For that purpose, the Operational Linescan System (OLS) was equipped with a two-band (0.6-μm visible and 11.0-μm thermal infrared window) imager useful for detection of low and high clouds. What makes the OLS unique is its extremely high sensitivity to low levels (e.g., down to 10^{-5} W · m^{-2} · sr^{-1} band-averaged radiance) of visible radiation, achieved via a high-gain amplifier (photomultiplier tube)—making it viable for an assortment of useful low-light feature-detection-oriented applications (see, e.g., [10]).

For example, in the case of detecting, at night, lower tropospheric clouds (e.g., having cloud-top pressures exceeding ~700 hPa), conventional satellite visible-band sensors provide no information, and infrared observations face considerable challenges (owing to low cloud-top temperatures being similar to the background clear-sky environment). Whereas multispectral techniques involving differences between the near-infrared 3.9-μm and thermal-infrared 11.0-μm bands demonstrate some ability to detect low-cloud decks at night by virtue of cloud spectral emissivity differences (see, e.g., [11]–[13]), these techniques may fail in the case of large cloud-top particle sizes (common to maritime stratus) and in regions of high-column water vapor. In contrast, OLS measurements of reflected moonlight reveal immediately these low-cloud structures, including exposed low-level circulation centers of tropical cyclones in formative/decay phases as in [14].

With its primary emphasis on contrast-based cloud detection, the OLS nighttime visible channel lacks attributes useful to quantitative applications. Its coarse radiometric resolution (6-bit data, or 64 gray shades) and lack of standard calibration (employing a dynamic highly variable scene/swath/lunar-cycle-dependent gain aimed at attaining maximum scene contrast [4]) relegate with very few exceptions its practical usage to qualitative imagery. In addition to these intrinsic sensor limitations, the OLS suffers from stray sunlight entering the telescope during certain parts of the season and portions of the orbit, causing diffuse light "solar glare" effects that contaminate and render useless significant portions of the data collected.

The National Polar-orbiting Operational Environmental Satellite System (NPOESS) program, a joint NOAA/NASA/ DoD venture to provide the U.S. with an operational constellation to succeed the NOAA-led Polar Orbiting Environmental Satellite program, will offer several new technologies— including an improved nighttime visible sensor capability that draws heritage from the DMSP/OLS. The NPOESS Visible/Infrared Imager/Radiometer Suite (VIIRS), a 22-band optical-spectrum radiometer suite, will include the Day/Night Band (DNB). The DNB introduces new technology capable of capturing a wide range of low-light signal at high spatial and radiometric resolution. The minimum radiance of the DNB (at highest stage gain and detector aggregation mode) is similar to the OLS, but the DNB has been designed to exceed the performance of the OLS both in spatial (0.74 km across entire swath) and radiometric (14 bit) resolution. These improvements, coupled with the multispectral complementary information from other collocated VIIRS channels, poise NPOESS to pursue quantitative applications heretofore restricted to daytime measurements—a true paradigm shift in nighttime remote sensing capability.

A high-quality measurement of upwelling radiance is of only limited use, however, if the measurement cannot be put into the context of a reflectance. A given measure of DNB radiance could be produced by a weakly reflecting target at high input light or a strongly reflecting target at low input light. Therefore, when considering measurements of reflected moonlight, we must constrain the magnitude of input light (downwelling irradiance) in order to understand the magnitude of reflectance, which is then related to various physical properties of the environment. For daytime visible-band sensors, the downwelling TOA solar spectral irradiance is well defined, with adjustments made over the course of the season to account primarily for S/E distance changes and, to a lesser extent, the minor variations associated with the ~11-year solar cycle. Moonlight, in contrast, is a highly variable quantity since the Moon itself is not a self-illuminating object; it simply reflects sunlight incident upon it. The illuminated portion (and associated irradiance output) of the Moon as viewed from the Earth varies (waxes/wanes) across the lunar cycle. In addition, the magnitude of TOA lunar irradiance at a given point in the lunar cycle varies from one cycle to the next (owing to the Moon's elliptical orbit) and across the seasons (elliptical Moon/Earth (M/E)-system orbit around the Sun). Without an accurate account for these variations, the DNB cannot realize its full potential as a nocturnal analog to the daytime visible channels.

This paper describes a lunar spectral irradiance database developed for the purpose of enabling lunar-reflectance-based nighttime environmental applications from the NPOESS/VIIRS DNB. Section II provides an overview of the theory and considerations behind this development, and Section III compares the current results to various point sources (e.g., satellite lunar calibrations). To provide a portable and computationally efficient version of the model, Section IV presents a standard version of the lunar spectral irradiance database (with error analysis) that allows for rapid interpolation to current S/E/M geometric conditions. Section V discusses limitations to the current lunar spectral irradiance database, and Section VI illuminates potential nighttime applications that are enabled by this information. Section VII concludes this paper.

II. BACKGROUND AND MODEL DEVELOPMENT

For the purposes of this paper, we consider the Moon as a source of visible radiation for nighttime sensing of the Earth's atmosphere and surface. In contrast to the interests of the astronomy community, the emphasis here is not on the detailed physics and chemistry of the lunar surface (except in the context of its bulk effect on the lunar spectral reflectance, or albedo). Over the decades, astronomers have collected many data from lunar albedo observations across the ultraviolet (UV)/visible/infrared spectrum useful for development of a lunar radiation model. There is an increase with wavelength of the lunar albedo across the UV part of the spectrum [15]. Numerous other studies of the lunar UV spectrum are provided by the authors in [16]–[20]. Data for the visible part of the spectrum are provided by Harris [23], and Dobber *et al.* [24], [25] provide additional data on the geometric albedo in the visible (and also UV) as well as information on the lunar phase function. With the advent of the U.S. space program, astronauts in the Gemini program measured radiation from the Moon in

the infrared part of the spectrum [26]. The infrared spectra for selected areas of the lunar surface viewed by telescope are provided by McCord and Johnson [27], and Shaw [28] provides a simple model for the lunar infrared. These and other observational data are summarized by Lane and Irvine [29].

A detailed analysis of the spectral albedo from the published results of many investigators compiled over a long period was used to build a composite set of albedo values for wavelengths from about 0.2 to 1.2 μm. In some cases, we communicated with the authors of the associated papers directly to clarify issues regarding their data collection and analysis. Curve fits to these data over two spectral subregions were produced for inclusion in the current lunar model. The resulting albedo curves match closely with the ensemble of published data upon which they are based and provide the most accurate spectral data for the geometric albedo of the Moon without account for libration effects. Whereas the albedo will depend on libration, such a refinement is considered as a point of future refinement to the model developed here. The geometric albedo presented here is considered as an average over all possible libration conditions.

Recent measurements of the radiation for the Moon have been performed by a number of groups who are interested in the lunar surface properties. Among these are lunar spectral radiance measurements collected by Paul Lucey *et al.* at the Hawaii Institute of geophysics and Planetology. By using the Extreme Universe Space Observatory (EUSO), the Europeans have generated data at the wavelength of 0.555 μm. These data are presented as a function of the lunar phase angle by Montanet [30]. Our current results compare favorably to EUSO data for conditions of both lunar perigee and apogee.

In addition, in recent years, a detailed series of measurements (over 85 000 lunar observations in the spectral range from 347 to 2390 nm) has been made by Kieffer and Stone [31] at the U.S. Geological Survey (USGS) in Flagstaff, AZ. Lunar libration is included implicitly in their data set because this is an empirical model based on actual measurements over an extended period of time and many lunar phases. They present a formula, with 328 coefficients based on these measurements, that calculates a phase-dependent lunar albedo. Thus, the phase function is included in their albedo as opposed to other descriptions of the lunar albedo that have only wavelength dependence. Their formula allows one to determine the albedo in terms of the selenographic latitude and longitude of the observer and the selenographic longitude of the Sun. The data are valid for lunar phase angles (θ_p, defined as the angle between the Earth and Sun as viewed from the Moon) from 0° to 90°.

Accurate representation of the TOA lunar spectral irradiance requires accounting for the following several factors: 1) changes in Sun/Moon (S/M) and M/E distances due to elliptical orbits; 2) variations of the lunar phase angle (which relate to what fraction of the Moon appears illuminated when viewed from the Earth); 3) intrinsic variations of the solar source; and 4) the heterogeneity of the lunar surface (both surface properties and lunar topography effects, e.g., crater shadows) which give rise to varying lunar reflectance with changing lunar phase angle and libration. These factors are discussed in more detail hereinafter. Geometric constants and other terms important to the calculation of the lunar spectral irradiance are provided in Table I.

TABLE I
CONSTANTS USED IN CALCULATION OF LUNAR SPECTRAL IRRADIANCE. ALL DISTANCES BETWEEN BODIES ARE FROM CENTER-OF-MASS TO CENTER-OF-MASS

Parameter	Symbol	Value and Units
Sun Radius	r_s	695,508 km
Moon Radius	r_m	1737.4 km
Earth Radius (Equatorial)	r_e	6378.14 km
Moon/Earth Perigee Distance	$R_{me,p}$	356,371 km
Moon/Earth Apogee Distance	$R_{me,a}$	406,720 km
Sun/Earth Perihelion Distance	$R_{se,p}$	147,088,067.2 km
Sun/Earth Aphelion Distance	$R_{se,a}$	152,104,233.4 km
Astronomical Unit	AU	149,597,870.7 km
Mean Sun/Earth Radius	$\overline{R}_{se}$	149,598,022.6 km
Mean Moon/Earth Radius	$\overline{R}_{me}$	384,401 km
Lunar Visual Albedo	α	0.116; 0.105<α<0.125
Total Solar Irradiance	E_o	1361 W-m^{-2} (at 1AU)

The elliptical orbits of the Earth about the Sun and the Moon about the Earth result in nonnegligible changes to the TOA lunar spectral irradiance. The minimum and maximum S/E distances (perihelion and aphelion, respectively) lead to varying amounts of sunlight incident on the lunar surface, and the minimum and maximum M/E distances (perigee and apogee, respectively) result in changes to the solid angle subtended by the Moon. Since the Moon is not a self-illuminating object, the lunar radiance will change primarily according to the S/M distance, and the lunar irradiance upon the Earth changes primarily according to Earth/Moon (E/M) distance.

Over the course of the lunar cycle, θ_p waxes from near 180° (New Moon) toward 0° (Full Moon) and then wanes back toward 180°, resulting in a variable illuminated fraction of the Moon over successive nights (Fig. 1). New Moons and Full Moons that occur when the Moon is directly in line with the Earth and Sun correspond to solar eclipses ($\theta_p = 180°$, Earth passes through the Moon's shadow) and lunar eclipses ($\theta_p = 0°$, Moon passes through the Earth's shadow), respectively. The inclination of the lunar orbit about the Earth with respect to the Earth's orbit about the Sun is about 5°, such that eclipses occur only on rare occasions. Although the same side of the Moon always faces the Earth (a sun-synchronous lunar rotational rate owing to the combination of frictional dissipation of the Moon's rotational energy and the gravitational force of the Earth), this finite inclination allows for slightly different parts of the Moon to be viewable.

These phase-angle-dependent variations in lunar brightness are taken into account implicitly within the lunar phase function $f(\theta_p)$. Varying between zero and one, the phase function describes the nonlinear behavior of lunar brightness with phase angle and can be applied as a multiplicative factor to the maximum possible lunar irradiance (i.e., a factor of unity would
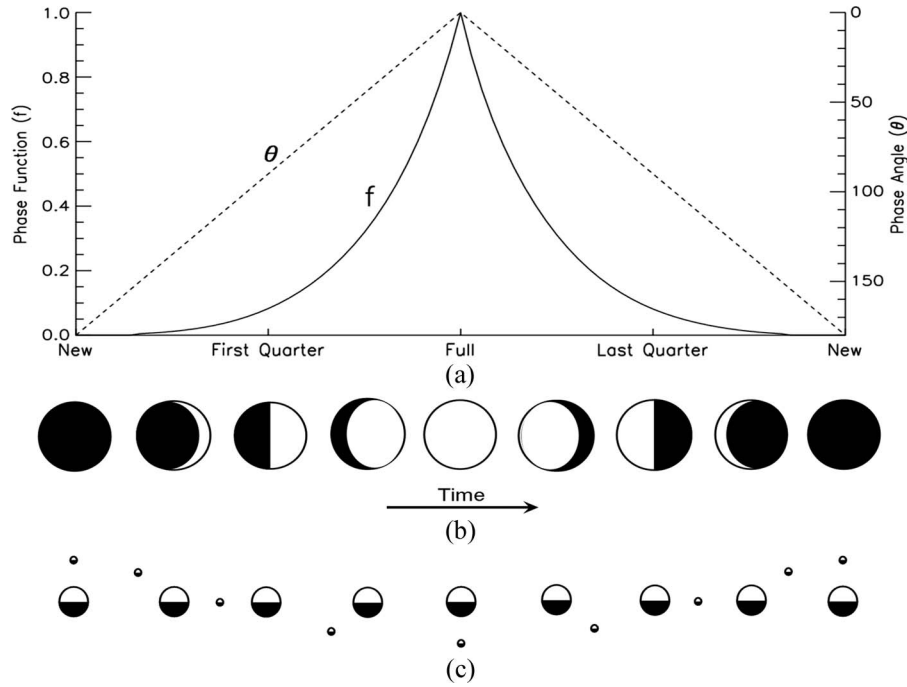
Fig. 1. (a) Evolution of the lunar phase angle (θ) and phase function (f) over the course of the lunar cycle. (b) Changing appearance of the lunar disk as shown from Earth. (c) E/M geometry (not drawn to scale) as viewed from a position above the North Pole of Earth (with sunlight originating from top of page). In (b) and (c), illuminated sides of bodies are shown in white and shaded sides in black.

TABLE II
LUNAR MAGNITUDES AS A FUNCTION OF PHASE ANGLE (ROWS, IN DEGREES) AND
WAVELENGTH (COLUMNS, IN NANOMETERS) FROM THE STUDY IN [29]

	359.0	392.6	415.5	457.3	501.2	626.4	729.7	859.5	1063.5
0°	0.0	0.0	0.0	0.0	0.0	0.0	0.0	0.0	0.0
10°	0.29	0.27	0.29	0.28	0.27	0.27	0.26	0.25	0.24
20°	0.58	0.55	0.57	0.56	0.55	0.53	0.52	0.50	0.48
30°	0.86	0.82	0.86	0.83	0.82	0.80	0.77	0.74	0.72
40°	1.15	1.09	1.15	1.11	1.10	1.06	1.03	0.99	0.96
50°	1.41	1.34	1.41	1.37	1.36	1.32	1.28	1.23	1.20
60°	1.66	1.60	1.67	1.62	1.62	1.58	1.54	1.49	1.44
70°	1.93	1.88	1.95	1.90	1.89	1.86	1.82	1.77	1.70
80°	2.23	2.19	2.26	2.20	2.20	2.17	2.13	2.08	1.99
90°	2.59	2.56	2.61	2.55	2.54	2.52	2.48	2.43	2.33
100°	3.01	2.99	3.02	2.95	2.94	2.93	2.87	2.82	2.72
110°	3.51	3.50	3.50	3.42	3.40	3.41	3.32	3.27	3.18
120°	4.11	4.10	4.06	3.98	3.94	3.97	3.83	3.78	3.72

correspond to $\theta_p = 0°$, the maximum solid angle of illuminated lunar disk viewable for a given M/E distance). As the phase angle approaches 0°, a reduction in crater shadows and increase in coherent backscattering result in a nonlinear increase in the apparent lunar brightness (roughly a 40%–45% increase between 5° and 0°)—a phenomenon known as the opposition effect (see, e.g., [32]). It should be pointed out that from the vantage point of the Earth, it is impossible to view a true Full Moon (i.e., $\theta_p = 0°$) phase angle since this would correspond to a lunar eclipse (the Moon crossing within the umbral shadow of Earth). For example, the total lunar eclipse on August 28, 2007 corresponded to a lunar phase angle of approximately 0.212°.

The phase functions used in the spectral lunar irradiance model were based on fits to the spectrally dependent phase functions in [29]. Their data were used to determine the magni-

tude of the lunar irradiance as a function of arbitrary wavelength and phase angle. The lunar magnitude (m) data (Table II) were fitted linearly as a function of wavelength (λ, in micrometers) and phase angle over the spectral range [0.3, 1.2 μm]

$$m(\theta_p, \lambda) = a(\theta_p) - b(\theta_p)\lambda \qquad (1)$$

where coefficients a and b (Table III) are functions of lunar phase angle (generated for 10° phase function increments from 10° to 120°). For a given wavelength and lunar phase angle, the model software interpolates to obtain the lunar magnitude, which is then used to evaluate the corresponding phase function according to

$$f(\theta_p, \lambda) = 10^{-0.4\,m}. \qquad (2)$$

TABLE III
LINEAR FIT COEFFICIENTS FOR EVALUATING LUNAR MAGNITUDE PER (1)

Phase angle	a	b
10°	0.30805	0.0652190
20°	0.61802	0.1336200
30°	0.92169	0.1989200
40°	1.23130	0.2668300
50°	1.50230	0.2961900
60°	1.76490	0.3078300
70°	2.04800	0.3204200
80°	2.36050	0.3320600
90°	2.72480	0.3540200
100°	3.15660	0.3995500
110°	3.66680	0.4609600
120°	4.27780	0.5570100

Values of the phase function evaluated at the same coordinates as in Table II are shown in Table IV. The interpolated phase functions compared favorably to observations collected at several phase angles. The response function of the DNB is spanned entirely by the data in [29], where correlation with the curve fits is high.

We take special care to point out that using the current model at very large phase angles (greater than about 120°) and at wavelengths below 360 nm or exceeding 1060 nm is not recommended, since calculations done in these regimes are based largely on extrapolation and the accuracy of the phase function has not been evaluated with sufficient observational data. In addition, through our use of data from [29], we do not account for the opposition surge (which, as described earlier, becomes an important source of uncertainty at phase angles less than about 5°). Whereas some lunar cycles never reach significantly low phase angles, others do and may remain so for several hours. The larger phase angles (exceeding ~120°) are deemed less important to nighttime satellite applications using the DNB, as they correspond to the period between New Moon and the First/Last Crescent Moons (when there is very little available moonlight) and over very small time-windows just prior to sunrise and immediately following sunset (when twilight contributions may dominate the visible light signal).

The conventional total solar irradiance (TSI) as measured at one astronomical unit (AU) (see Table I) is roughly 1366 W · m^{-2}. This "solar constant," in fact, varies over time by several watts per square meter, owing to various fluctuations within the photosphere of the Sun (e.g., the 11-year sunspot cycle). Measurements of the solar spectral irradiance by ground-based instruments and satellite instruments continue as researchers attempt to reconcile the differences among various sensor characteristics and agree upon a "standard" solar spectrum. A summary paper on the TSI is given by Frohlich and Lean [33], and analysis of the spectral variability for the mid- and near-UV parts of the spectrum that is the most variable is conducted by Lean *et al.* [34]. The current work enlists solar spectral radiance data from the Solar Radiation and Climate Experiment (SORCE). These data have been continuous since 2003. The SORCE-derived TSI, 1361 W · m^{-2}, is slightly lower than the older convention. The solar spectral radiance data used in the current model (which are integrated over the geometry-dependent solid angle subtended by the Sun for a given simulation to provide spectral irradiance) are an average of the solar maximum and the solar minimum values from SORCE data (publicly available at http://lasp.colorado.edu/sorce/index.htm) and are provided in the supplemental materials.[1]

The primary variation in TOA downwelling solar irradiance is due to the Earth's elliptical orbit, which results in an approximately ±3.4% spread about the TSI (ranging between 1320 and 1412 W · m^{-2}) over the course of the year. The intrinsic change in the TSI, excluding geometric variations, is about 0.1%. While these extrinsic and intrinsic changes to the solar output are small, they must be accounted for when working with high radiometric resolution observations.

The geometric lunar spectral albedo (α_λ, integrated over the entire surface) values used for the current model are based on composite data from numerous sources (see [28], [35], and [36], among others cited at the beginning of this section), and the model calculations of the subsequent irradiances compare favorably (e.g., agreement within 2%–6% across the visible spectrum) to satellite-measured lunar irradiance. These spectral data were represented in the model by curve fits over two spectral bands according to

$$\alpha(\lambda) = \sum_{i=0}^{n} A_i \lambda^i \tag{3}$$

with fit coefficients A_i provided in Table V. Fig. 2 shows the geometric lunar spectral albedo along with the solar spectral irradiance at 1 AU. Of note is the low value of mean lunar albedo ($\overline{\alpha} = 0.116$, integrated between 0.4 and 0.7 μm and weighted/normalized by solar spectral irradiance)—surprisingly less than that of Earth ($\overline{\alpha}_E \approx 0.30$). The Moon being perceived as a very bright object in the nighttime sky is, in fact, the result of its strong contrast against the dark (space) background.

III. MODEL THEORY

The solar irradiance incident upon the Moon at arbitrary S/M distance is given by

$$E_m = E_o \left(\frac{\overline{R}_{\text{se}}}{R_{\text{sm}}} \right)^2 \tag{4}$$

where E_o is the solar constant, $\overline{R}_{\text{se}}$ is the mean S/E radius, and R_{sm} is the S/M distance (which varies over the course of both the lunar cycle and the seasons), This incident irradiance is reflected by the Moon according to the geometric lunar albedo (α), producing an equivalent isotropic radiance that is given by

$$L_m = \frac{\alpha E_m}{\pi} \tag{5}$$

that is then integrated over the solid angle of the illuminated portion of the lunar disk (phase dependent) as viewed from the Earth to compute the downwelling lunar irradiance. If lunar surface heterogeneities are captured to first order by the geometric lunar albedo and phase function, the TOA lunar spectral

---

[1]This paper has supplementary downloadable material available at http://ieeexplore.ieee.org, provided by the authors. Spectral solar radiance data derived from the SOlar Radiation and Climate Experiment (SORCE), averaged from the solar maximum and minimum values observed. The dataset is 19 kB in size.

TABLE IV
LUNAR PHASE FUNCTION AS A FUNCTION OF PHASE ANGLE (ROWS, IN DEGREES) AND
WAVELENGTH (COLUMNS, IN NANOMETERS) FROM THE STUDY IN [29]

	359.0	392.6	415.5	457.3	501.2	626.4	729.7	859.5	1063.5
0°	1.0	1.0	1.0	1.0	1.0	1.0	1.0	1.0	1.0
10°	0.7656	0.7798	0.7656	0.7727	0.7798	0.7798	0.7870	0.7943	0.8017
20°	0.5861	0.6026	0.5916	0.5970	0.6026	0.6138	0.6194	0.6310	0.6427
30°	0.4529	0.4699	0.4529	0.4656	0.4699	0.4786	0.4920	0.5058	0.5152
40°	0.3467	0.3664	0.3467	0.3597	0.3631	0.3767	0.3873	0.4018	0.4130
50°	0.2729	0.2911	0.2729	0.2832	0.2858	0.2965	0.3076	0.3221	0.3311
60°	0.2168	0.2291	0.2148	0.2249	0.2249	0.2333	0.2421	0.2535	0.2655
70°	0.1690	0.1770	0.1660	0.1738	0.1754	0.1803	0.1871	0.1959	0.2089
80°	0.1282	0.1330	0.1247	0.1318	0.1318	0.1355	0.1406	0.1472	0.1600
90°	0.0920	0.0946	0.0904	0.0955	0.0964	0.0982	0.1019	0.1067	0.1169
100°	0.0625	0.0637	0.0619	0.0661	0.0667	0.0673	0.0711	0.0745	0.0817
110°	0.0394	0.0398	0.0398	0.0429	0.0437	0.0433	0.0470	0.0492	0.0535
120°	0.0227	0.0229	0.0238	0.0256	0.0265	0.0258	0.0294	0.0308	0.0325

TABLE V
EXPANSION COEFFICIENTS FOR SPECTRAL LUNAR ALBEDO
PER (3), BROKEN DOWN OVER TWO SPECTRAL BANDS

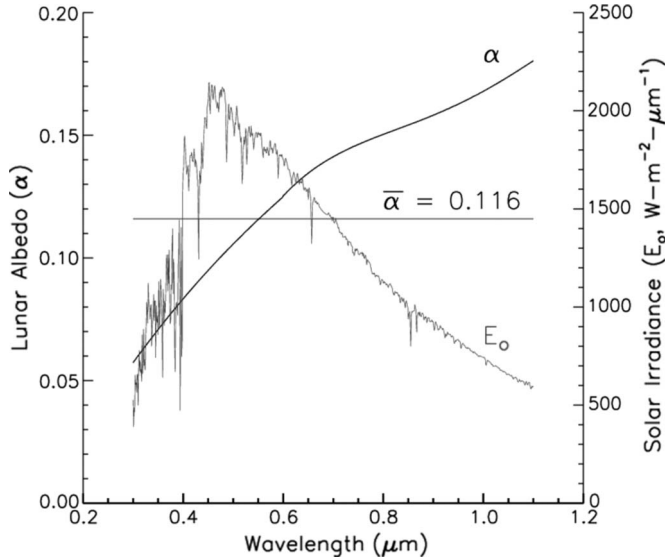|	$0.30 < \lambda < 0.60 \ \mu m$	$0.60 \leq \lambda < 1.20 \ \mu m$
A_0	-4.944×10^{-2}	-7.317×10^{-1}
A_1	4.406×10^{-1}	3.621
A_2	-3.150×10^{-1}	-5.656
A_3	1.084×10^{-1}	3.934
A_4	---	-9.999×10^{-1}

Fig. 2. Solar spectral irradiance (E_o) and spatially averaged lunar spectral albedo (α) across the Visible and SWIR. The spectral mean value of α (shown as horizontal line) is weighted by E_o.

irradiance upon the Earth can be expressed as the product of the lunar radiance and the solid angle subtended by the full lunar disk

$$E_{\text{TOA}} = L_m \Omega_m = \alpha E_o \left(\frac{\overline{R}_{\text{se}}}{R_{\text{sm}}} \right)^2 \left(\frac{r_m}{R_{\text{me}} - r_e} \right)^2 f(\theta_p) \quad (6)$$

where R_{sm} varies slightly as a function of the phase angle. This irradiance is expressed in units of watts per square meter per unit wavelength by using the spectrally resolved values for albedo, solar irradiance, and phase function. The downwelling component of the lunar irradiance at a particular time and location on the Earth's surface can then be computed by multiplying by the cosine of the lunar zenith angle (information available from ephemeris software such as the U.S. Naval Observatory's Multiyear Interactive Computer Almanac: 1990–2005; http://aa.usno.navy.mil/software/mica/micainfo.html).

A. Sensitivity to Extremes in Orbital Geometry

Assuming again, for simplicity, the case of a Full Moon (such that $R_{\text{sm}} = R_{\text{se}} + R_{\text{me}}$), we can evaluate (6) at the extremes of the S/E/M geometries to determine the dynamic range of possible E_{TOA}. The minimum, maximum, and mean values for E_{TOA} follow by substituting for R_{me} values corresponding to apogee, perigee, and mean M/E distance, respectively, and likewise substituting for R_{se} values corresponding to aphelion, perihelion, and mean S/E distance, respectively. Table VI lists the minimum, maximum, and mean radiances and irradiances (integrated across the spectrum) defining the range of possible values for Full Moons viewed from Earth.

We can evaluate the range of possible E_{TOA} by taking the ratio between the maximum and minimum values produced at [aphelion/apogee] and [perihelion/perigee], respectively

$$E^* = \frac{E_{\text{TOA}}(Max)}{E_{\text{TOA}}(Min)} = \left(\frac{R_{\text{se},a} + R_{\text{me},a}}{R_{\text{se},p} + R_{\text{me},p}} \right)^2 \left(\frac{R_{\text{me},a} - r_e}{R_{\text{me},p} - r_e} \right)^2. \quad (7)$$

Substituting the constants defined in Table VI, we find that $E_{\text{TOA}}(Max)$ is approximately 1.4 times $E_{\text{TOA}}(Min)$. The corresponding percentage change is 33.32%, representing the greatest possible percent change in lunar irradiance arising from S/E/M geometry variations. Holding the M/E distance at its mean value, the change is 6.69% (representing the variation due to changes of distance between the Sun and the Earth). Similarly, fixing the S/E distance such that we consider only the variations in M/E distance, we capture roughly the complement (26.79%) of the total variation. The aforementioned operations are, in fact, coupled since variations in lunar radiance (which

TABLE VI
MINIMUM (APOGEE/APHELION), MAXIMUM (PERIGEE/PERIHELION), AND MEAN
VALUES OF LUNAR RADIANCE AND IRRADIANCE FOR A FULL MOON

	Apogee, Aphelion	Perigee, Perihelion	$\bar{r}_{me}$, 1 AU
Radiance (W-m^{-2}-sr^{-1})	4.728×10^{1}	5.055×10^{1}	4.889×10^{1}
Irradiance (W-m^{-2})	2.797×10^{-3}	3.916×10^{-3}	3.244×10^{-3}

go on to describe TOA lunar irradiance via solid angle) are tied to the S/M distance and not the S/E distance. This accounts for the small excess of the summed components with respect to the total variation. By this analysis, we see that the primary variation in TOA lunar irradiance for a given phase is the solid angle subtended by the Moon, as determined by the M/E distance. This effect is about four times larger than the variation due to proximity to the Sun.

Repeating this exercise (again, for $f = 1$) in terms of lunar radiance, specified as

$$L_M = \frac{E_{\text{TOA}}}{\Omega_M} = \frac{\alpha E_o}{\pi} \left(\frac{\overline{R}_{\text{se}}}{R_{\text{se}} + R_{\text{me}}} \right)^2 \qquad (8)$$

we find a 6.75% change in the total radiance between the extreme distance cases (perihelion/perigee versus aphelion/apogee). Alternatively holding fixed the M/E and S/E distances (to determine the relative contributions of each), we find that the S/E distance accounts for more than 99.93% of this total variation. Again, the small residual ($\sim$0.07%) variation contained in the M/E component is due to minor coupling between the terms being held fixed, in this case, the associated distance change between the Sun and the Moon when changing from apogee to perigee. As expected, the lunar radiance at a given phase angle (neglecting libration effects on the lunar albedo) is determined almost entirely by the variable S/M distance.

IV. VALIDATION

Calculations of lunar spectral irradiance by the current model were compared against independent calculations, experimental data sets, and a collection of low-Earth-orbiting satellite imaging radiometer Moon views. Given the very high photometric stability of the lunar surface ($\sim$10^6 years [37]), the Moon represents an excellent target for vicarious calibration. Lunar views are collected monthly for on-orbit calibration purposes by instruments such as the Sea-viewing Wide Field-of-view Sensor (SeaWiFS) (see, e.g., [38] and [39]) and MODIS (see, e.g., [40] and [41]). Since its launch in 1997, SeaWiFS has completed over 100 lunar calibration maneuvers via an instrument pitch change at opportune positions in its orbit. Using the lunar reflectance as a calibration reference for the visible-near infrared (VNIR) bands on the NPOESS Preparatory Project (NPP) VIIRS sensor is also being considered (see [42]).

Fig. 3 shows percent-difference comparisons between observed and predicted (using the current work) lunar spectral radiances for an assortment of MODIS and SeaWiFS reflective band lunar calibration maneuvers. Data were obtained from the MODIS Characterization Support Team (http://www.mcst.ssai.biz/mcstweb/index.html) and via Bob Eplee (per-
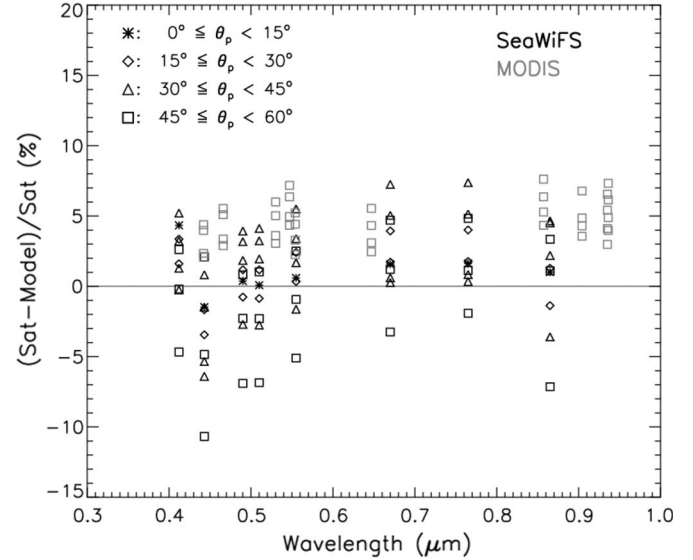

Fig. 3. Comparisons between the current model and lunar views by SeaWiFS (dark-black symbols) and Aqua MODIS (light-gray symbols) for selected sensor bands across the Visible and SWIR. Symbols correspond to different lunar phase angle regimes ranging roughly from gibbous to nearly full.

sonal communication, using the data set described in [39]) for SeaWiFS. The various symbols denote different lunar phase angle regimes, partitioned into 15° increments, and are positioned on the central wavelength of the satellite instrument bands (for MODIS, only angles in the neighborhood of 55° are available). For the model calculations, the lunar solid angle was adjusted to match satellite altitude (i.e., substitution of Moon–spacecraft distance for M/E distance). Typical agreement is within 5%, with slightly better performance observed for the low lunar phase angle cases. This performance is considered reasonable in light of there being no corrections/adjustments made to the observations to account for libration and sensor oversampling effects (see, e.g., [39]). There do not appear to be any significant wavelength or lunar phase angle biases, although MODIS comparisons indicate a systematic positive bias (satellite radiances brighter than predicted) that may be related to the way spectral averages were computed for the instrumentation.

The RObotic Lunar Observatory (ROLO) (see [31]) is a USGS-sponsored project aimed at using the Moon as a calibration standard for remote sensing satellites. Located at the USGS Science Center in Flagstaff, AZ (32.21° N, 111.63° W, 2.15-km altitude) and operating since the late 1990s, ROLO houses an extensive database of clear-sky lunar radiance imagery ($> 85\,000$ distinct views for specific regions of the lunar surface) from VNIR (23 bands) and shortwave infrared (SWIR) (9 bands) camera sensors (see [31, Table 1]). Starlight is used to approximate the atmospheric extinction and correct the surface-based measurements to TOA-equivalent values, and absolute

TABLE VII
COMPARISON BETWEEN LUNAR SPECTRAL IRRADIANCE (E_λ, GIVEN IN MILLIWATTS PER SQUARE METER PER MICROMETER) CALCULATED FROM CURRENT WORK AND ROLO FOR SELECTED WAVELENGTHS AND LUNAR PHASE ANGLES

λ(nm)	θ_p (degrees)	Lunar Illum (%)	E_λ (Current)	E_λ (ROLO)	% Diff
350	2.862	99.938	1.370	1.604	14.59
350	34.683	91.119	0.498	0.483	3.15
544	3.924	99.883	4.320	4.530	4.64
544	50.070	82.088	1.214	1.189	2.10
1243	2.862	99.938	2.089	2.226	6.15
1243	34.683	91.119	0.907	0.849	6.84

calibration is tied to astronomical photometry of the star Vega and National Institute of Standards and Technology calibration spheres. From these photometric observational data, an empirically based (analytical functions) lunar irradiance model is derived. ROLO represents accurate values for the lunar albedo in terms of various selenographic coordinates with higher precision for specific spectral bands. We have made comparisons of our model with calculations in the ROLO project and generally found good agreement as a function of phase angle. The only significant disagreement seems to be near a phase angle of zero, which is understandable because of the difficulties in analyzing the opposition effect. Table VII shows comparisons between ROLO and the current work for selected wavelengths and lunar phase angles.

It is important to make the distinction here between ROLO and the current work in order to clarify the point that the two methods are not competing; the objectives and applications of the data are entirely different. The intent of ROLO is to provide highly accurate vicarious calibration data for satellite sensors. In contrast, the aim of the current work is to provide a generalized method for calculating the lunar spectral irradiance at 1-nm spectral resolution as a function of time for any date, with the intent being to convolve these data with a sensor response function to yield TOA downwelling irradiance at any location/time. In order to use the ROLO data in this mode, it would be necessary to determine the phase angle as a function of time for all 32 wavelength bands in their database and then perform interpolations over roughly 800 spectral values to fill in the high-resolution database.

An additional issue is that of selenographic coordinate variation (i.e., sub-Earth latitude and longitude on the lunar surface) due to lunar libration. These coordinates differ from year to year. We seek values for the integrated disk of the Moon, meaning that the selenographic coordinates would have to be calculated according to date and time. While certainly this can be done for the full model, we cannot apply the results in the context of a scaling relationship based on the "standard-geometry" approach described in Section V. For this reason, we use spectral albedo data compiled from measurements by many observers and the spectral phase function data based on the band-averaged values in [29].

V. STANDARD-GEOMETRY LUT

Operational algorithms using moonlight measurements require a fast, generalized, and self-consistent approach for computing lunar spectral irradiance across the instrument bandpass. The specific intent of this lunar spectral irradiance model was for automated near real-time processing of environmental applications from the NPOESS/VIIRS DNB. To run the full model on every DNB pixel (0.74-km resolution and a 3000-km swath width) would require over 4000 subroutine calls per scan line. Doing so is impractical, computationally inefficient, and superfluous in light of the minimal changes in TOA lunar irradiance (arising from subtle changes in the apparent lunar phase angle) compared to the magnitude of uncertainties in the current model. In the interest of portability/ distribution and speed of calculation (for integration within automated processing systems), a simple lookup table (LUT) version of the model is provided. The table is based on a standard S/E/M geometry and geocentric viewing assumptions using an auxiliary table of time-dependent variables for scaling the results to current geometries.

The standard tables were defined for mean S/E distance (1 AU) and mean M/E distance (see Table I). The only degree of freedom is the varying position of Moon in its orbit around the Earth (i.e., the varying lunar phase angle, neglecting libration effects). If the standard LUT (using geometry) can be represented following the same construct as (6)

$$\overline{E}_{\text{TOA}} = \alpha E_o \left(\frac{\overline{R}_{\text{se}}}{\overline{R}_{\text{sm}}}\right)^2 \left(\frac{r_m}{\overline{R}_{\text{me}} - r_e}\right)^2 f(\theta_m) \qquad (9)$$

then the adjustment factor used to convert from standard distances to a current S/E/M geometry is the ratio between (6) and (9), i.e.,

$$F = \left(\frac{\overline{R}_{\text{sm}}}{R_{\text{sm}}}\right)^2 \left(\frac{\overline{R}_{\text{me}} - r_e}{R_{\text{me}} - r_e}\right)^2. \qquad (10)$$

Provided tables of lunar phase angle, S/E distance, and M/E distance as a function of time, the current S/M distance may be calculated via the cosine law as follows:

$$R_{\text{sm}} = \sqrt{(R_{\text{se}}^2 + R_{\text{me}}^2 + 2R_{\text{se}}R_{\text{me}}\cos(\theta_p))}. \qquad (11)$$

Since the distance between the Moon and Earth is very small compared to the distance between either body and the Sun, (10) can be rewritten to a good approximation in a form that is independent of the lunar phase angle

$$F = \left(\frac{\overline{R}_{\text{se}}}{R_{\text{se}}}\right)^2 \left(\frac{\overline{R}_{\text{me}} - r_e}{R_{\text{me}} - r_e}\right)^2. \qquad (12)$$

The standard tables were calculated at 1° resolution in lunar phase angle. Results for selected lunar phase angles are shown in Fig. 4, along with the VIIRS-DNB spectral response function (SRF). Correction terms [see (10)] corresponding to the extreme conditions of apogee/aphelion and perigee/perihelion applied to the bold standard curves show the possible spread in the solution space arising from geometric considerations. A comparison of the exact and standard lunar irradiance at 600 nm for the waxing mode of the lunar cycle, shown in
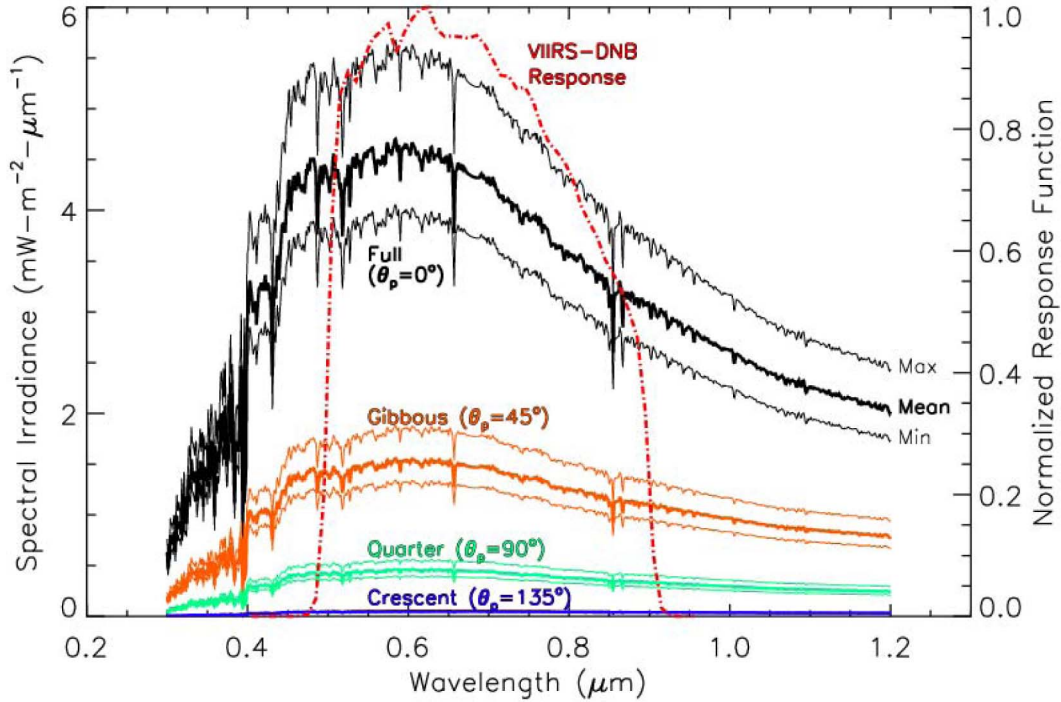
Fig. 4. Results from the standard lunar spectral irradiance tables for selected lunar phase angles ranging from Crescent to Full Moon (from Miller and Turner, 2008). Heavy curves ("Mean") correspond to the standard geometry (1 AU, mean M/E distance). Light curves ("Max" and "Min") correspond to perigee/perihelion and apogee/aphelion geometries, respectively. The VIIRS-DNB SRF is shown as a red dashed-dot curve.

Fig. 5 (for a case near mean S/E/M geometry), confirms very close agreement (typically within 0.05%) even after the approximation introduced in (12). Repeating this exercise at other S/E/M geometries, including the extremes of apogee/aphelion and perigee/perihelion (not shown), yielded similar results.

A. Using the Standard Table

The intended use of the standard table described earlier is rapid calculation of the absolute (i.e., unweighted by the SRF of a particular sensor) downwelling TOA lunar irradiance at any given date, time, and location. The required information for making this calculation is the current S/E distance, M/E distance, and lunar phase angle. A precomputed auxiliary data set containing hourly values for these quantities is supplied with the standard tables. An example procedure for applying these data to a sensor with arbitrary SRF confined to the spectral interval [0.3, 1.2 μm] is as follows.

1) Convolve standard-table lunar spectral irradiance data with the SRF to yield a sensor-specific TOA lunar irradiance table (at 1° phase angle resolution), e.g.,

$$E(\theta_p)_{\text{TOA}} = \frac{\int_{\lambda} E_{\text{TOA}}(\lambda, \theta_p)\phi(\lambda)d\lambda}{\int_{\lambda} \phi(\lambda)d\lambda}. \quad (13)$$

2) Given the current date and time, interpolate the auxiliary data set to obtain the corresponding S/E and M/E distances and lunar phase angle information.
3) Linearly interpolate the convolved irradiance table from Step 1) to the phase angle determined in Step 2).

4) Scale the interpolated irradiance from Step 3) using (12) and the current S/E and M/E distances and lunar phase angle obtained from Step 2).
5) Scale the irradiance according to the cosine of the local lunar zenith angle.

Software and auxiliary data sets required to carry out the aforementioned procedure for the NPOESS VIIRS/DNB have been made available as supplementary material[2] (see the Conclusion section for additional information).

An example of the standard table lunar spectral irradiance convolved with the normalized SRF (i.e., Step 1) of the procedure described earlier) of both the VIIRS/DNB and the DMSP/OLS is shown in Fig. 6. The values correspond roughly to the mean curves shown in Fig. 4 for an effective center wavelength near 680 nm. Differences between the OLS and DNB curves at low phase angles (between Quarter and Full Moon) are 2%–3%. Similar results may be computed for any future nighttime-visible sensor, provided that the SRF is contained fully within the spectral range of the current database.

VI. MODEL LIMITATIONS

The convenience of a fast and general approach to the calculation of lunar spectral irradiance for the purposes of operational applications comes at the expense of some tradeoffs in accuracy. These approximations, combined with nonnegligible uncertainties in some aspects of the observational data sets

---

[2]This paper has supplementary downloadable material available at http://ieeexplore.ieee.org, provided by the authors. Datasets and code to compute the top-of-atmosphere down-welling lunar irradiance convolved to the preliminary NPOSS/VIIRS DNB spectral response function. This material is 11 MB in size.
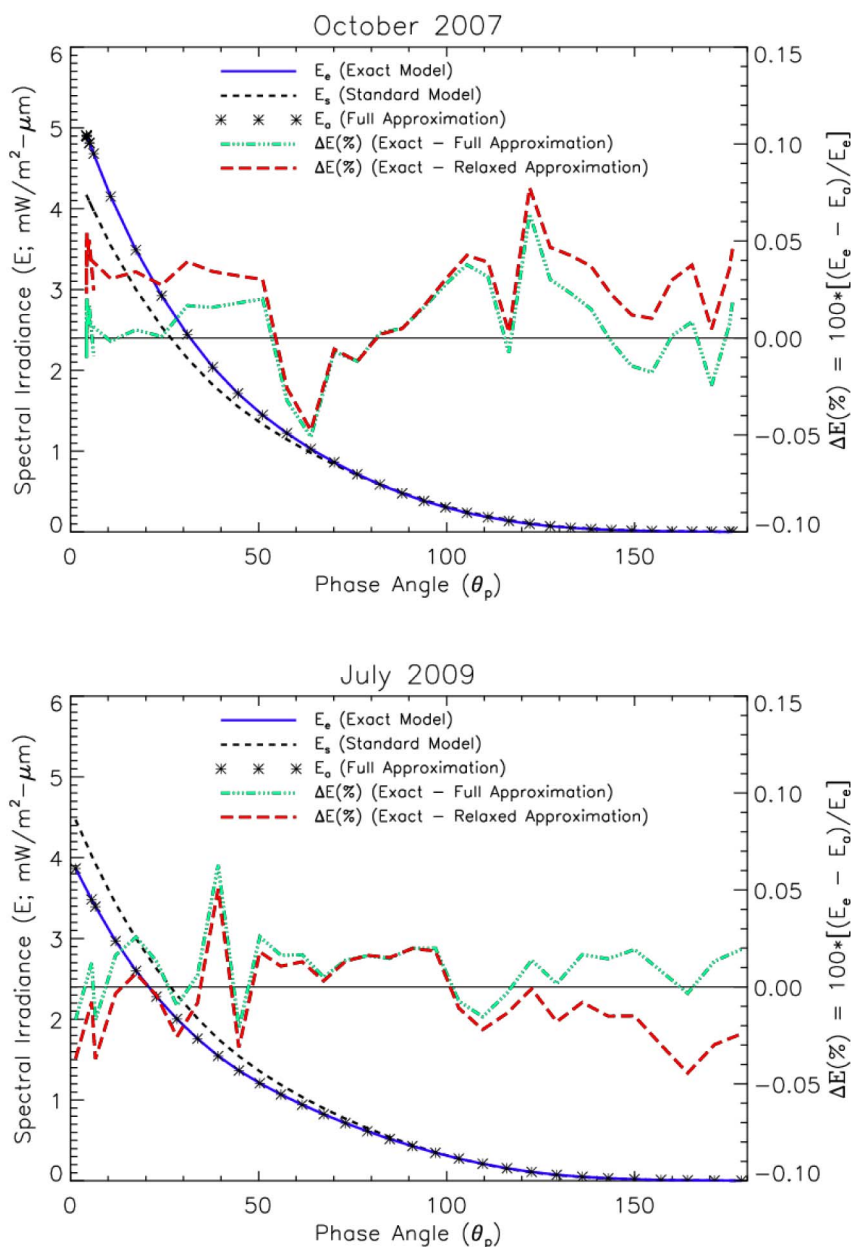
Fig. 5. Comparison between the standard (using mean S/E and E/M distances) lunar irradiance model and exact calculations at $\lambda = 600$ nm for (top) perigee/perihelion case and (bottom) apogee/aphelion case. Percent differences between exact and adjusted standard models using the conversion factors described in the text.

themselves, warrant specific highlighting. Enumerated here are some of the more important compromises made by the current work along with inherent uncertainties in the state-of-the-art observational data upon which parts of the current model are based.

1) There is some uncertainty in the lunar phase function, due primarily to lunar spectral and spatial reflectance variability (i.e., a heterogeneous surface). Few new measurements currently are being made of the lunar phase function, particularly as a function of wavelength. Such work requires a concerted effort over an extended period of time, with careful attention paid to the atmospheric corrections if done using ground-based telescopes. Based on the usage of data from [29], there is an uncertainty

of 0.1% per degree of lunar phase angle. There will be greater errors for lunar phase angles exceeding 120°. As explained previously, only a small illuminated portion the Moon is visible at these higher phase angles, so there is minimal impact to most nighttime applications based on lunar reflectance where observations are sparse.

2) Owing to spherical geometry, lunar topography, and surface heterogeneity, the actual brightness of the Moon varies nonlinearly with the phase angle. Lunar features such as dark basaltic *maria* basins and lighter colored *terrae* highlands result in slightly different apparent lunar brightness (and, hence, TOA lunar irradiance) for identical phase angles on the waxing versus waning side. Based on differences between curve fits to the empirical data in [43] for waxing and waning modes (not shown here),
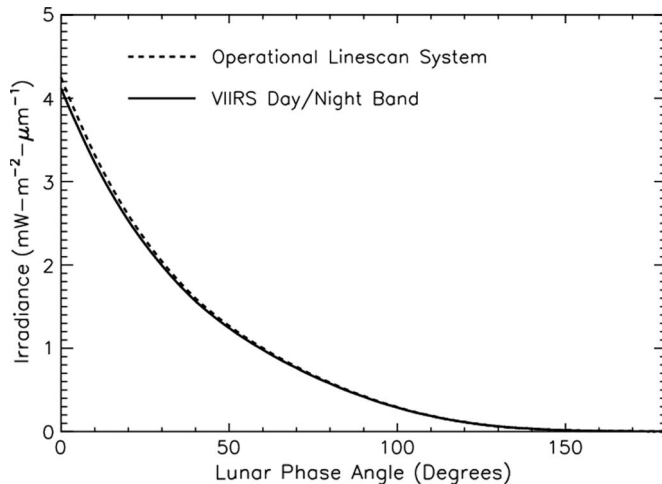
Fig. 6. Standard-geometry (S/E distance of 1 AU and mean M/E distance) lunar spectral irradiance convolved with the normalized sensor response functions of the VIIRS DNB (and the current DMSP-OLS sensor, for comparison), shown as a function of lunar phase angle.

the waxing Moon is found to be approximately 2%–3% brighter than the waning Moon at significant phase angles ($\theta_p < 90°$, consistent with lunar photography that shows a greater proportion of *maria* located on the western side of the lunar disk).

3) Some disagreement between the current work and ROLO in the shortwave/UV (< 400 nm) suggests possible disparities either in the lunar spectral albedo or solar source at these wavelengths. In any case, these departures are not an issue for the targeted VIIRS-DNB application since the sensor response function has negligible sensitivity to the UV portion of the spectrum. In general, agreement to within 5% was found. Although none of the methods represent absolute truth, they provide some sense of consistency.

4) Not accounting for the opposition effect will result in growing uncertainties for lunar phase angles less than about 5°. The lunar opposition effect is of considerable interest to astronomers, and research is ongoing. Several investigators have attempted to model the opposition effect from a theoretical point of view, with varying degrees of success (see, e.g., [44]–[46]). Since these issues have not yet been addressed comprehensively as a function of wavelength, we have not included them in this work. It is worthwhile, however, to be aware of developments in this field for possible inclusion in a future version of the model. For the purposes of nighttime environmental applications from NPOESS/VIIRS, these uncertainties will only be significant for a relatively small part of the time near a lunar eclipse, so it is taken as negligible in most cases.

5) The current model does not account for libration effects on the lunar albedo: The Moon is in a synchronous orbit with the Earth, such that roughly the same lunar surface faces the Earth throughout its orbit. However, a 6.687° obliquity of the lunar orbit to Earth's equatorial plane results in slightly different faces of the Moon being observable from Earth over time (up to 59% of the total surface area, instead of just 50%). The work of

Eplee *et al.* [39] (cf. Fig. 10) suggests that we incur a $\pm 2\%$ error due to this effect. A libration correction could be added in a time-dependent tabular form in a future release of this lunar irradiance table.

6) Variability of the solar constant (TSI) was not included in this work. This could be an addition to the LUT in a future release (i.e., a simple scaling of E_o based on current solar observations). Whereas the large geometric annual variation is well accounted for in the current model, the long-range intrinsic solar variability is a subject of ongoing research as next-generation satellite observing systems will continue to monitor the solar irradiance. The 11-year solar cycle can be modeled, but this variation is small and was not included in this model. Based on the study in [47], the variation in the TSI is estimated as 0.2%, with the majority of the variance occurring at UV wavelengths that are outside the sensitivity range of the VIIRS DNB.

7) Research continues in the determination of the lunar spectral albedo. In this paper, we have put together what we believe are the best data to obtain a composite spectral albedo from a large number of experiments and comprising many years of observation. The uncertainties in this compilation are estimated to be 2%–6%. Future satellite and ground-based measurements of the lunar radiation will provide updates to the current results.

8) When using standard-geometry table, the date and time of interest are used to compute the distances and lunar phase. This approach necessarily provides the phase angle for a *geocentric* geometry and, thus, is only completely valid for the sublunar point on the Earth surface. To assess the uncertainty here, we computed for a test case (June 21, 2003) the normal lunar irradiance for a range of longitudes over the entire range for all lunar zenith angles along the equator and found the maximum difference to be about 2.8%. This represents the maximum change in the lunar irradiance between an observer at moonrise and the point for an observer at the sublunar point and therefore an additional source of uncertainty when using the standard-geometry table results. The "exact geometry" model, which includes front-end software for calculating the detailed lunar geometry and phase function for any observer location, allows for topocentric calculations and avoidance of this 2.8% uncertainty.

Based on these estimates, an overall uncertainty on the order of 7%–17% should be anticipated from the current model, with the higher end values corresponding to high ($> 120°$) and very low ($< 5°$) phase angles. For the majority of data collected by the VIIRS DNB, an uncertainty of 7%–12% is expected, with higher end values corresponding to the usage of the standard-geometry LUT. Uncertainties or on-orbit changes in the VIIRS-DNB sensor response function used to convolve with these spectral lunar irradiance data will be addressed via on-board and/or vicarious calibration techniques when this information becomes available. The current lunar irradiance data, produced at 1-nm spectral resolution, allow for recalculation should the response function be found to differ dramatically from what was assumed. These uncertainties are not included in the assessment of model uncertainty.

It is important to note that the algorithms leveraging these lunar spectral irradiance data for nighttime environmental applications contain uncertainties that often are much larger than the uncertainties associated with the irradiance data themselves. For example, radiative transfer models of cloudy or aerosol-laden atmospheres, which would use lunar irradiance as a system input for reflectance calculations in a physical retrieval framework, very often assume simple plane parallel geometry (e.g., neglecting 3-D effects such as shadowing and sub-pixel-scale variability), single layers, idealized particle size distributions and microphysics, simplified lower boundary (surface) properties, etc. Just a subset of these forward model assumptions can lead to errors in retrieved properties on the order of several tens of percent and in some cases higher for cloud optical property retrievals [48]. Nevertheless, the value added from lunar irradiance information in terms of enabling these and other nighttime applications in most cases outweighs the detraction due to inherent forward model inaccuracies. The following section highlights some of the applications enabled or improved upon by the availability of a nighttime visible sensor coupled with knowledge of the downwelling TOA lunar spectral irradiance.

VII. ENVIRONMENTAL APPLICATIONS OF NIGHTTIME VISIBLE DATA

With its calibrated, multigain, high spatial, and radiometric resolution measurements, combined with its collocation with multiple channels on VIIRS, the DNB represents a paradigm shift from the legacy DMSP/OLS system. Although the primary role of the DNB [from the perspective of NPOESS Environmental Data Records (EDRs)] is simply to provide continuity to the DMSP/OLS in terms of near-constant contrast imagery, its unique capability stands to extend its utility to a large number of NPOESS EDRs and enable others not included.

For example, cloud detection and classification algorithms, based in part on visible reflectance thresholds during the day, often face challenges at night. This is true particularly for low clouds exhibiting weak temperature contrast against the background and weak spectral (emissivity) contrast owing to large cloud-top droplet sizes. OLS data demonstrate qualitatively how the detection of these clouds is improved at night by moonlight reflection (see, e.g., [14]). In addition, the coupling of visible reflectance and the "split-window" (11 and 12 μm) channels can be used to determine thin cirrus over low-cloud overlap situations (important information for cloud property retrievals) [49].

Fig. 7 shows both concepts based on OLS imagery for a complex cloud scene over the Gulf of Mexico. The top panel demonstrates the low-cloud detection capabilities (low clouds depicted in red and cirrus in cyan) of conventional infrared-only techniques. The lower panel shows roughly the same scene observed with the inclusion moonlight reflectance (with low clouds now depicted in yellow and cirrus in blue), revealing a low-cloud deck hidden beneath a thin cirrus shield over southern Texas and a portion of the eastern Gulf, and improved low-cloud detection over the Yucatan Peninsula and parts of the Caribbean. Discrete bright yellow patches in the lower panel are the light emissions from large cities, which preclude moonlight-based techniques. With knowledge of the downwelling lunar
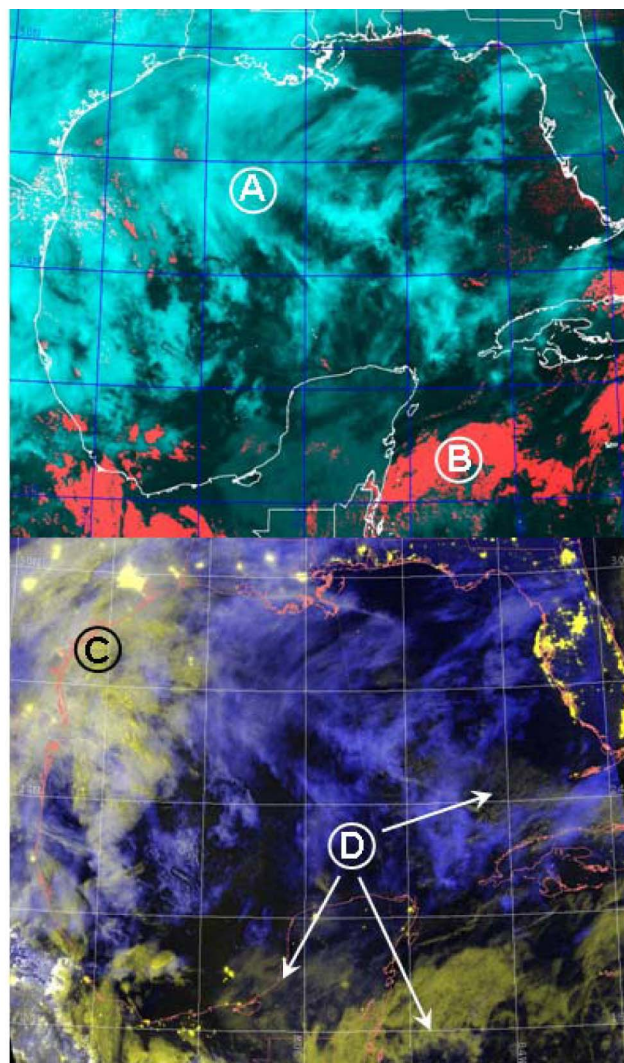

Fig. 7. Nighttime cloud detection from conventional infrared-only observing systems (top: GOES-East, January 30, 2007 at 0145 UTC, cirrus clouds in cyan [A] and low-level water clouds in red [B]), and a nighttime visible+infrared system (bottom: F-15 OLS same date at 0157 UTC, with cirrus in blue and the low clouds in yellow). Label A shows a thin cirrus shield obscuring a low-cloud deck that is revealed by moonlight near Label C. Label D denotes areas where moonlight improves the detection of some low clouds missed by the infrared-only method. Knowledge of the lunar reflectance will improve quantitative algorithms for general cloud detection at night and enable new capabilities for nighttime cloud overlap identification.

irradiance, DNB information can be incorporated within the VIIRS cloud mask/type algorithms in a quantitative way to improve the performance of these EDRs when moonlight is available.

With the availability of visible reflectance data, cloud optical depth (related to the column-integrated cloud water content) can be retrieved over a broader range and accuracy in comparison to conventional nighttime methods relying exclusively on near-infrared and thermal-infrared. This improvement is due to the fact that clouds are highly emissive in the infrared and thus saturate rapidly in their brightness temperatures with increasing optical depth in contrast to the highly scattering nature of clouds in the visible part of the spectrum. Here, lunar reflectance provides greater sensitivity to changes in optical thickness and, hence, the total cloud water content. Similarly, lunar reflectance

can aid in the detection and characterization of tenuous aerosol layers over dark backgrounds.

Algorithms invoking reflectance-based thresholds, made possible through knowledge of the downwelling lunar irradiance, include the nighttime mapping of sea ice and snow cover. The 0.74-km spatial resolution, nearly constant across the ~3000-km VIIRS swath width, will be sufficient in most cases to identify and alert ships to hazardous icebergs in polar waters. A nighttime NPOESS pass over a previously cloud-obscured region may provide the first opportunity to reveal a freshly deposited snow field. Operational users will no longer need to wait until the first morning satellite passes for this information.

In addition, there are a variety of environmental applications reliant on measurement of visible light emissions from the surface or atmosphere whose pursuit requires minimal levels of external light contamination. Examples here include the detection of aeroral boundaries, active (flaming) fires, bioluminescence, and lightning flashes. The work of Zhang *et al.* [9] demonstrates a concept for obtaining of aerosol optical depth from comparisons between city lights on clear and turbid nights, and the work of Miller *et al.* [7] requires the absence of moonlight for detection of luminous bacterial emissions at the lower end of instrument sensitivity. Other applications can be pursued in the presence of moonlight, if it is sufficiently low compared to terrestrial emission signal. For such applications, the presence of moonlight effectively raises the noise floor, and the algorithm-specific threshold for signal-to-noise ratio requires quantitative knowledge of the incoming moonlight. The lunar irradiance information developed in the current work (together with local lunar geometry information that is to be included in the VIIRS-DNB data stream) could be used here to determine the limiting conditions where and when such applications could be pursued.

VIII. CONCLUSION

A lunar spectral irradiance database created at 1-nm resolution across the spectral range [0.3, 1.2 μm] has been developed to enable quantitative applications of the VIIRS DNB. To make these data practical to future developers of nighttime applications, a standard LUT based on mean S/E and M/E distances was produced, together with auxiliary data tables that are used to adjust these standard-geometry values to the specific S/E/M geometry of current observations. The resultant TOA downwelling lunar spectral irradiance can be used in an analogous way to TOA solar spectral irradiance (i.e., enabling the computation of scene reflectance), enabling numerous quantitative cloud/aerosol/surface applications confined heretofore to daytime passes exclusively. The uncertainties attached to the model, including the geocentric assumption of the standard-geometry model, range from 7% to 12% for typical observing conditions. The information must be coupled with auxiliary information on the lunar geometry (zenith, relative azimuth angles) at a particular location on the Earth's surface.

The first DNB will be included on the NPP, slated for launch in mid-2010. As implied by its name, the purpose of the NPP is to serve as risk reduction for the novel suite of NPOESS sensors and affording the user community an opportunity to prepare for the new operational data stream. Similar to previous satellite observing systems such as MODIS,

SeaWiFS, and the Advanced Microwave Scanning Radiometer (AMSR-E), however, timely NPP data will, in all likelihood, be leveraged for operational support purposes. The main goals of this research were to raise awareness in the community to the largely untapped potential (from an NPOESS-EDR capability standpoint) of the VIIRS-DNB sensor and to supply developers with a tool well in advance of the NPP program. The standard-geometry lunar spectral irradiance database, auxiliary data, and example software for calculating the lunar spectral irradiance for both unweighted (absolute) and the specific case of the VIIRS/DNB sensor as a function of date/time are available online at http://ieeexplore.ieee.org.

REFERENCES

[1] T. A. Croft, "Burning waste gas in oil fields," *Nature*, vol. 245, no. 5425, pp. 375–376, Oct. 1973.

[2] R. Welch, "Monitoring urban population and energy utilization patterns from satellite data," *Remote Sens. Environ.*, vol. 9, no. 1, pp. 1–9, Feb. 1980.

[3] C. D. Elvidge, K. E. Bauhg, E. A. Kihn, H. W. Kroehl, and E. R. Davis, "Mapping city lights with nighttime data from the DMSP operational linescan system," *Photogramm. Eng. Remote Sens.*, vol. 63, no. 6, pp. 727–734, Jun. 1997.

[4] C. D. Elvidge, K. E. Baugh, J. B. Dietz, T. Bland, P. C. Sutton, and H. W. Kroehl, "Radiance calibration of DMSP-OLS low-light imaging data of human settlements," *Remote Sens. Environ.*, vol. 68, no. 1, pp. 77–88, Apr. 1999.

[5] C. D. Elvidge, P. Cinzano, D. R. Pettit, J. Arvesen, P. Sutton, C. Small, R. Nemani, T. Longcore, C. Rich, J. Safran, J. Weeks, and S. Ebener, "The Nightsat mission concept," *Int. J. Remote Sens.*, vol. 28, no. 12, pp. 2645–2670, Jan. 2007.

[6] J. L. Foster, "Observations of the Earth using nighttime visible imagery," *Int. J. Remote Sens.*, vol. 4, pp. 785–791, 1983.

[7] S. D. Miller, S. H. D. Haddock, C. Elvidge, and T. F. Lee, "Detection of a bioluminescent milky sea from space," *Proc. Nat. Acad. Sci.*, vol. 102, no. 40, pp. 14 181–14 184, 2005.

[8] S. D. Miller, T. F. Lee, F. J. Turk, A. P. Kuciauskas, and J. D. Hawkins, "Shedding new light on nocturnal monitoring of the environment with the VIIRS day/night band," *Proc. SPIE*, vol. 5890, p. 589 00W, 2005.

[9] J. Zhang, J. S. Reid, S. D. Miller, and F. J. Turk, "Strategy for studying nocturnal aerosol optical depth using artificial lights," *Int. J. Remote Sens.*, vol. 29, no. 16, pp. 4599–4613, Aug. 2008.

[10] T. F. Lee, S. D. Miller, F. J. Turk, C. Schueler, R. Julian, S. Deyo, P. Dills, and S. Wang, "The NPOESS/VIIRS day/night visible sensor," *Bull. Amer. Meteorol. Soc.*, vol. 87, no. 2, pp. 191–199, Feb. 2006.

[11] R. P. d'Entremont, "Low- and midlevel cloud analysis using nighttime multispectral imagery," *J. Appl. Meteorol.*, vol. 25, no. 12, pp. 1853–1869, Dec. 1986.

[12] G. P. Ellrod, "Advances in the detection and analysis of fog at night using GOES multispectral infrared imagery," *Weather Forecast.*, vol. 10, no. 3, pp. 606–619, Sep. 1995.

[13] T. F. Lee, F. J. Turk, and K. Richardson, "Stratus and fog products using GOES-8-9 3.9 μm data," *Weather Forecast.*, vol. 12, no. 3, pp. 664–677, Sep. 1997.

[14] S. D. Miller, J. D. Hawkins, K. Richardson, T. F. Lee, and F. J. Turk, "Enhanced tropical cyclone monitoring with MODIS and OLS," in *Proc. 27th Hurr. Trop. Meteor. Conf. Amer. Meteor. Soc.*, 2006, 15A.6. CD-ROM.

[15] R. Stair and R. Johnston, "Ultraviolet spectral radiant energy reflected from the Moon," *J. Res. Natl. Bur. Stand.*, vol. 51, no. 2, pp. 81–84, 1953.

[16] I. A. Ahmad and W. A. Deutschman, "Ultraviolet photometry of the moon with the celescope experiment on the OAO-II," *Astron. J.*, vol. 77, no. 8, pp. 692–694, Oct. 1972.

[17] A. N. Bentley, C. G. De Jonckheere, and D. E. Miller, "Geometric albedo of the Moon in the ultraviolet," *Astron. J.*, vol. 79, no. 3, pp. 401–403, Mar. 1974.

[18] R. L. Lucke, R. C. Henry, and W. G. Fastie, "Far-ultraviolet albedo of the Moon," *Astron. J.*, vol. 81, no. 12, pp. 1162–1169, Dec. 1976.

[19] H. H. Wu and A. L. Broadfoot, "The extreme ultraviolet albedos of the planet Mercury and of the Moon," *J. Geophys. Res.*, vol. 82, no. 5, pp. 759–761, 1977.

[20] R. C. Henry, P. D. Feldman, J. W. Kruk, A. F. Davidson, and S. Durrence, "Ultraviolet albedo of the moon with the Hopkins Ultraviolet Telescope," *Astrophys. J.*, vol. 454, pp. L69–L72, Nov. 1995.

[21] G. R. Gladstone, J. S. McDonald, W. T. Boyd, and S. Bowyer, "EUVE photometric observations of the moon," *Geophys. Res. Lett.*, vol. 21, no. 6, pp. 461–464, 1994.

[22] S. J. Janz, E. Hilsenrath, R. P. Cebula, and T. J. Kelly, "Observations of the lunar geometric albedo during the ATLAS-3 mission," *Geophys. Res. Lett.*, vol. 23, no. 17, pp. 2297–2300, 1996.

[23] D. L. Harris, "Photometry and colorimetry of planet and satellites," in *Planet and Satellites*, G. P. Kuiper and B. M. Middlehurst, Eds. Chicago, IL: Univ. Chicago, 1961.

[24] M. R. Dobber, "GOME Moon measurements, including instrument characteristics and Moon albedo," in *Proc. 3rd ERS Symp. Space Service Environ.*, 1997, pp. 743–747, ESA SP-414.

[25] M. R. Dobber, A. P. H. Goede, and J. P. Burrows, "Observations of the global ozone monitoring experiment: Radiometric calibration and lunar albedo," *Appl. Opt.*, vol. 37, no. 33, pp. 7832–7841, Nov. 1998.

[26] T. P. Condron, J. J. Lovett, W. H. Barnes, L. Marcotte, and R. Nadile, *Gemini 7 Lunar Measurements.* Bedford, MA: Air Force Cambridge Res. Labs., Office Aerosp. Res., U.S. Air Force, 1968. AFCRL-68-0438, Environmental Research Paper 291.

[27] T. B. McCord and T. V. Johnson, "Lunar spectral reflectivity (0.03 to 2.50 microns) and implications for remote mineralogical analysis," *Science*, vol. 169, no. 3948, pp. 855–858, Aug. 1970.

[28] J. A. Shaw, "Modeling infrared lunar radiance," *Opt. Eng.*, vol. 38, no. 10, pp. 1763–1764, Oct. 1999.

[29] A. Lane and W. Irvine, "Monochromatic phase curves and albedos for the lunar disk," *Astron. J.*, vol. 78, no. 3, pp. 267–277, Apr. 1973.

[30] F. Montanet, "EUSO duty cycle: Moon and Sun light effects," *EUSO-SIM-REP-009-1.3*, 2006. Issue 1, Revision 3.

[31] H. H. Kieffer and T. C. Stone, "The spectral irradiance of the Moon," *Astron. J.*, vol. 129, no. 6, pp. 2887–2901, 2005.

[32] B. J. Buratti, J. K. Hillier, and M. Wang, "The lunar opposition surge: Observations by Clementine," *Icarus*, vol. 124, no. 2, pp. 490–499, Dec. 1996.

[33] C. Fröhlich and J. Lean, "Total solar irradiance variations: The construction of a composite and its comparison with models," in *Proc. IAU Symp. 185: New Eyes See Inside Sun Stars*, F. L. Deubner, Ed., 1995, pp. 89–102.

[34] J. L. Lean, G. J. Rothman, H. L. Kyle, T. N. Woods, J. R. Hickey, and L. C. Puga, "Detection and parameterization of variations in solar mid- and near-ultraviolet radiation (200–400 nm)," *J. Geophys. Res.*, vol. 102, no. D25, pp. 29 939–29 956, Dec. 1997.

[35] R. L. Younkin, "Optical reflectance of local areas of the Moon," *Astron. J.*, vol. 75, no. 7, pp. 831–840, Sep. 1970.

[36] S. J. Lawrence, E. Lau, D. Steutel, J. D. Stopar, B. B. Wilcox, and P. G. Lucey, "A new measurement of the absolute spectral reflectance of the Moon," in *Lunar Planet. Sci. XXXIV, Abstract 1269.* Houston, TX: Lunar and Planetary Institute, 2003. CD-ROM.

[37] H. H. Kieffer, "Photometric stability of the lunar surface," *Icarus*, vol. 130, no. 2, pp. 323–327, Dec. 1997.

[38] R. A. Barnes, R. E. Eplee, Jr., F. S. Patt, and C. R. McClain, "Changes in the radiometric sensitivity of SeaWiFS determined from lunar and solar-based measurements," *Appl. Opt.*, vol. 38, no. 21, pp. 4649–4664, Jul. 1999.

[39] R. E. Eplee, Jr., R. A. Barnes, F. S. Patt, G. Meister, and C. R. McClain, "SeaWiFS lunar calibration methodology after six years on orbit," *Proc. SPIE*, vol. 5542, pp. 1–13, 2004. 5542-2.

[40] J. Sun, X. Xiong, B. Guenther, and W. Barnes, "Radiometric stability monitoring of the MODIS solar reflective bands using the Moon," *Metrologia*, vol. 40, no. 1, pp. S85–S88, Feb. 2003.

[41] J. Sun, X. Xiong, W. L. Barnes, and B. Guenther, "MODIS reflective solar bands on-orbit lunar calibration," *IEEE Trans. Geosci. Remote Sens.*, vol. 45, no. 7, pp. 2383–2393, Jul. 2007.

[42] F. S. Patt, R. E. Eplee, R. A. Barnes, G. Meister, and J. J. Butler, "Use of the Moon as a calibration reference for NPP VIIRS," *Proc. SPIE*, vol. 5882, pp. 385–396, 2005. 5882-43.

[43] A. Rougier, "Total photoelectric photometry of the Moon," *Ann. Obs. Starsbourg*, vol. 2, pp. 205–339, 1933.

[44] B. Hapke, "Bidirectional reflectance spectroscopy," *Icarus*, vol. 67, no. 2, pp. 264–280, Aug. 1986.

[45] P. Helfenstein and J. Veverka, "Photometric properties of lunar terrains derived from Hapke's equation," *Icarus*, vol. 72, no. 2, pp. 342–357, Nov. 1987.

[46] P. Helfenstein, J. Veverka, and J. Hillier, "The lunar opposition effect: A test of alternative models," *Icarus*, vol. 128, no. 1, pp. 2–14, Jul. 1997.

[47] C. Fröhlich, "Observations of irradiance variations," *Space Sci. Rev.*, vol. 94, no. 1/2, pp. 15–24, Nov. 2000.

[48] S. D. Miller, G. L. Stephens, C. K. Drummond, A. K. Heidinger, and P. T. Partain, "A multisensor diagnostic cloud property retrieval scheme," *J. Geophys. Res.*, vol. 105, no. D15, pp. 19 955–19 971, 2000.

[49] M. J. Pavolonis and A. K. Heidinger, "Daytime cloud overlap detection from AVHRR and VIIRS," *J. Appl. Meteorol.*, vol. 43, no. 5, pp. 762–778, May 2004.

Steven D. Miller received the B.S. degree in electrical and computer engineering from the University of California, San Diego, in 1995 and the M.S. and Ph.D. degrees in atmospheric science from Colorado State University (CSU), Fort Collins, in 1997 and 2000, respectively.

From 2000 to 2007, he was with the Naval Research Laboratory, Monterey, CA, where he developed value-added satellite applications for operational users (including mineral dust, snow cover, cloud optical properties, low-cloud/fog, fire detection, deep convection, natural color imagery, contrails, volcanic ash, and nighttime low-light imagery). In 2007, he joined the Cooperative Institute for Research in the Atmosphere, Fort Collins, working on research and application development for current and future environmental satellite observing systems, with emphasis on the GOES-R and NPOESS programs. His research interests include satellite-based remote sensing of the Earth/atmosphere system from a wide assortment of active and passive observing systems spanning the optical to microwave portions of the electromagnetic spectrum.

Robert E. Turner received the B.S. and M.S. degrees in physics from the University of Cincinnati, Cincinnati, OH, in 1959 and 1960, respectively, the M.A. degree in physics from Columbia University, New York, in 1963, and the Ph.D. degree in physics from Washington University, St. Louis, MO, in 1970.

He has been with NASA, where he worked on mathematical models of stellar evolution. He has also been with the University of Michigan, Ann Arbor, and the Environmental Research Institute of Michigan, where he developed mathematical models to account for the transfer of visible and infrared through clouds and the atmosphere. He is currently with Science Applications International Corporation, Monterey, CA, where he continues to develop models for radiative transfer problems in smoke, dust, and natural water clouds. He also works on the transfer of laser radiation in multiple-scattering media and nonlinear optics. In recent years, he has developed models to account for ultraviolet, visible, and infrared radiation from starlight, the Moon, zodiacal light and airglow, and the creation of 3-D radiation models for clouds. He was a Principal Investigator on Skylab and Space Station projects and a Co-Investigator on Landsat. His research interests include radiative transfer problems related to multiple-scattering media, transport of high-energy cosmic rays through interstellar media, nuclear physics, satellite remote sensing of Earth resources using multispectral data methods, and solar system astrophysics.